ACS APPLIED MATERIALS & INTERFACES

www.acsami.org

Research Article

Protective Role of Oxides on Pb-Free Halide Perovskite Surfaces: Interfacial Effects and Excitonic Optical Properties from First-Principles

Maurizia Palummo,* Costanza Borghesi, Azusa Muraoka, Suraya Shaban, Shuzi Hayase, Daniele Varsano, Koichi Yamashita, and Giacomo Giorgi*

Cite This: ACS Appl. Mater. Interfaces 2026, 18, 32782−32794

Read Online

ACCESS | Metrics & More | Article Recommendations | Supporting Information

ABSTRACT: In this work, the impact of a GeO_2 overlayer on the stability and optoelectronic properties of Pb-free $Cs(Sn_{1-x}Ge_x)I_3$ perovskites is systematically investigated using first-principles calculations. Ge incorporation is found to substantially reduce the exciton binding energy relative to pristine $CsSnI_3$, thereby promoting more efficient electron−hole separation and enhancing the potential for carrier extraction. Guided by this trend, $Cs(Sn_{1-x}Ge_x)I_3$ (x = 0.25) slab models exposing the stable (001) surface were constructed, and both CsI- and MI_2-terminated facets (M = Sn, Ge, as well as Ge-only) were examined. The resulting perovskite/GeO_2 heterointerfaces display a pronounced dependence of structural rearrangements and band edge alignment on both composition and termination, allowing the identification of specific configurations that best preserve the desirable optoelectronic response. To better mirror experimental conditions, crystalline interface models were complemented by amorphous GeO_2 structures, thus capturing the structural complexity of realistic germania capping layers. Taken together, these results provide a microscopic picture of how GeO_2 overlayers can stabilize (Sn,Ge)-based halide perovskites while retaining electronic characteristics compatible with high-efficiency photovoltaic operation.

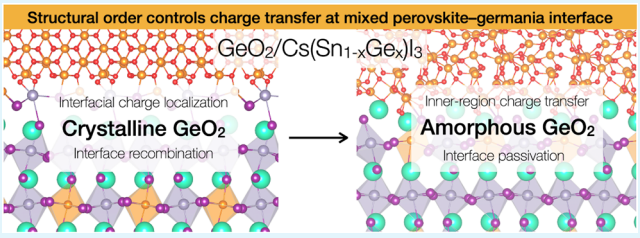

KEYWORDS: *photoconversion, optoelectronic properties, solar energy, crystalline interface models*

INTRODUCTION

Hybrid organic−inorganic halide perovskites (OIHPs) represent the major breakthrough in solar energy conversion over the last decades.[1] From the very initial work of Miyasaka et al.,[2] where the suitability of 3D bulk OIHPs in photoconversion has been demonstrated, new unprecedented photoconversion efficiencies (PCEs) have been reported, which nowadays reach and pass 26%.[3] Such class of compounds, characterized by the stoichiometric relationship ABX_3 (A = short-chain organic cation, usually $CH_3NH_3^+$ and $HC(NH_2)_2^+$; B = Pb^{2+}, Sn^{2+}, and less commonly Ge^{2+}; X = halides) embodies a series of features[4−7] that confer unique photoconversion properties, such as long carrier diffusion and lifetime, and not secondarily, an extremely low cost of processability.[8] Several papers and reviews have been published since 2009 aiming at characterizing—both experimentally and theoretically—such extraordinary class of compounds (see, e.g., among the many refs [9,10]). Many studies have been devoted to address the two intertwined issues that continue to hinder the large-scale exploitation of 3D organic−inorganic halide perovskites (OIHPs) in commercial devices, i.e., (i) the presence of a toxic element in the B-site of the compounds and (ii) the inherent instability of the 3D bulk class of compounds toward heat and moisture. The latter is enhanced by the volatility due to the presence of short-chain, *highly hydrophilic* organic moieties in the A-site. To mitigate this instability, a dimensionality-reduction strategy, from 3D to mixed 3D/2D or fully 2D systems, has been thus suggested.[11−19] Although this approach generally implies a modest reduction in power conversion efficiency (PCE), state-of-the-art values remain remarkably high, reaching 22% in alternating cations in the interlayer space (ACI) architectures[20] and up to 24.35% in the Ruddlesden−Popper motif.[21] This strategy consists on replacing short-chain organic cations with longer, *highly hydrophobic* aliphatic (e.g., butylammonium, BA = $CH_3(CH_2)_3NH_3^+$) or aromatic (e.g., phenethylammonium, PEA = $C_6H_5(CH_2)_2NH_3^+$) cations, which significantly enhance the structural stability of the resulting mixed-dimensional systems.

Beyond structural concerns, the environmental challenge of lead remains critical and probably the most tedious to solve.

Received: January 13, 2026
Revised: June 1, 2026
Accepted: June 3, 2026
Published: June 8, 2026

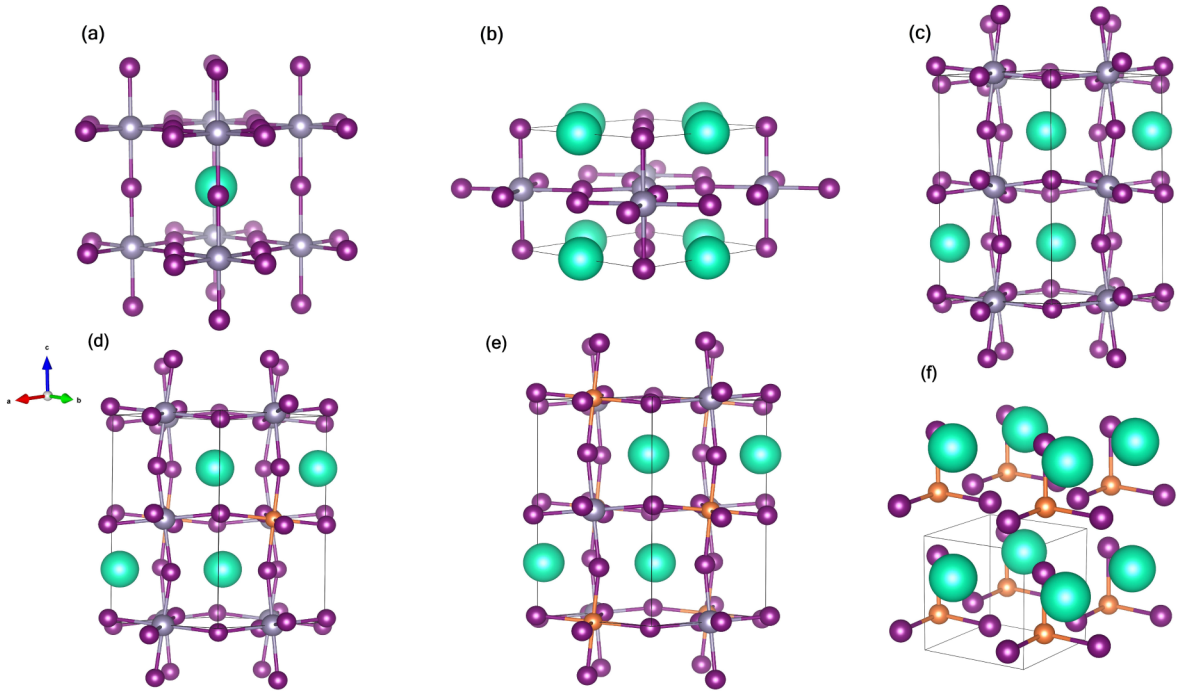

Figure 1. PAW/PBE-optimized atomic structure of (a) cubic, α- (b) tetragonal, β, (c) orthorhombic, γ-$CsSnI_3$, (d) $Cs(Sn_{1-x}Ge_x)I_3$ (x = 0.25), (e) $Cs(Sn_{1-x}Ge_x)I_3$ (x = 0.50) alloyed systems, (f) (2 × 2 × 2) supercell of $CsGeI_3$ [Mauve: Sn; Orange: Ge; Purple: I; Cyan: Cs atoms].

Efforts to address this issue have primarily focused on two strategies: homovalent replacement of Pb with Sn (either fully or partially—see, e.g., among the others, refs [22,23]), and heterovalent substitution of Pb pairs with two metallic centers with +1/+3 oxidation state.[24−29] Both processes suffer from side effects that potentially limit their applications. Sn at the B-site oxidizes to the +4 state more readily than Pb, accelerating the degradation of the perovskite solar cell (PSC). On the other hand, two different metals that occupy 50% of the B-site can decrease the dispersion of the band edge,[30−32] inducing reduced performance of the final PSC. However, attention has turned to mixed +2 oxidation state B-site halide perovskites (HPs),[33] and in particular to Sn-based ones. Indeed, forming solid solutions with Ge has been reported to improve the final alloyed system, compared to pristine Sn-based. While, indeed, pure germanium HPs[34] face intrinsic limitations as solar harvester, stemming from a marked lone-pair effect and for their bandgap slightly larger than that of Pb and Sn counterparts,[35] on the other hand, introducing Ge into Sn-based ones has been demonstrated to confer stability and improve the overall optoelectronic features. In this scenario, Hayase et al., mixing cations in both the A-site (FA, MA) and the B-site (Sn,Ge), proposed at first a (Sn,Ge)-mixed series of HPs whose bandgaps, measured by photoacoustic spectroscopy, fall within the optimal range for single-junction solar devices (1.40−1.53 eV). This finding supports the applicability of such mixed systems in solar cells: as reported, ∼5% doping Ge into the perovskite improves the efficiency up to 4.48% without encapsulation and, interestingly, upon doping the (Sn,Ge)-mixed HPs retain 80% of the original performance.[36] Still Hayase et al.[37] studied the role GeI_2 in (Sn,Ge)-mixed PSCs reporting an overall reduced device trap densities (10^{15}−10^{17} cm^{-3} when no Ge is added to 10^{8}−10^{14} cm^{-3} when 5% of Ge is added), long-lived carrier lifetime (τ = 5.04 ns), higher mobility (98.27 $cm^2V^{-1}s^{-1}$), longer diffusion length (>1 μm), and a final PCE of 7.9%. Here, authors ascribe the overall improvements in such mixed systems to the ability of Ge atoms to passivate the trap states. The impact of the different transparent conductive oxide substrates on the (Sn,Ge)-mixed PSCs has been investigated by Hamada et al.,[38] along with a comparison between inverted and standard structure: exploiting fluorine-doped tin oxide as a substrate led to a noticeable increase of the final efficiency of the PSC from 7.72% to 9.24%.

On the theoretical side, Zhou et al.[39] by means of a combination of standard DFT calculations both exploiting pure and hybrid functionals, report a complete description on the defect formation in such (Sn,Ge)-alloyed HPs. In detail, for different concentrations of Ge in $Cs(Ge_{1-x}Sn_x)I_3$, they found that the formation of antisites (I_{Sn} and I_{Ge}) may have a beneficial impact on the final properties of the x = 0.5 system due to the combined effect of alloying on both band edges and defect states. Focusing on the role played by the native oxide (GeO_2) formed at the surface of $CsSn_{0.5}Ge_{0.5}I_3$ mixed perovskite, Chen et al.[40] have demonstrated the benign effects of such formation on the overall working principle of the final device: the utilization of these perovskites is primarily driven by their exceptional stability, which stems from the spontaneous formation of a robust native germania layer. This ultrathin passivation layer effectively encapsulates and protects the perovskite surfaces, mitigating degradation pathways. Still, the authors demonstrate that alloying with Ge(II) in $CsSnI_3$ markedly enhances both stability and air tolerance. The rapid formation of a uniform native oxide surface layer on the mixed perovskite provides superior passivation, outperforming even the benchmark $MAPbI_3$ perovskite under ambient conditions. As a result, $CsSn_{0.5}Ge_{0.5}I_3$ solid-solution HPs may be exploited in PSCs reaching a PCE of 7.11% and are stable upon continuous operation under 1-sun illumination for over 500 h. Despite the growing interest in (Sn,Ge)-alloyed perovskites due to their appealing properties, our understanding of their chemistry remains limited. Even less is known about the mechanisms

https://doi.org/10.1021/acsami.6c00873
ACS Appl. Mater. Interfaces 2026, 18, 32782−32794

underlying their remarkable stability, particularly the surprising passivation effect provided by native oxide formation.[40,41] Accordingly, we consider it mandatory to further shed light on these systems paying particular attention to the properties of such (Sn,Ge)-alloyed HP surfaces, in their reactivity toward oxidizing agents and, last but not least, to the interfaces formed with native oxides, i.e., GeO_2.[40] Clearly, our focus is not the growth of oxide, which we cannot theoretically mimic by means of standard DFT calculations: in view of their potential implementation in PV, we study and theoretically characterize the structural and electronic features of the final coupled perovskite/germania systems. To the best of our knowledge, this work is one of the first to focus on the theoretical study of the interface between halide perovskites and oxide compounds.

COMPUTATIONAL DETAILS

Ground-state density functional theory (DFT) calculations were performed using the Vienna ab initio simulation package (VASP).[42−45] The Generalized Gradient Approximation (GGA), as parametrized by Perdew, Burke, and Ernzerhof (PBE),[46] was used to calculate the exchange-correlation (XC) energy. The projector augmented wave (PAW) potentials[47,48] were similarly used along with an energy cutoff of 600 eV. The semiempirical DFT-D3 corrections with Becke−Johnson damping[49,50] were included to account for van der Waals interactions. The Brillouin Zone (BZ) of the different systems was sampled with Γ-centered grids of different mesh, according to the size of the system: in particular, an 8 × 8 × 6 grid was used for optimizing the bulk orthorhombic γ-$CsSnI_3$ pristine cell and $Cs(Sn_{1-x}Ge_x)I_3$ (x = 0.25, 0.50) alloyed systems, while a 12 × 12 × 16 one was used for rutile GeO_2 (hereafter r-GeO_2, ($P4_2/mnm$)). The atomic positions and bulk lattice parameters of all the materials considered ($CsSnI_3$, $CsGeI_3$, $Cs(Sn_{1-x}Ge_x)I_3$ (x = 0.25, 0.50), and GeO_2) were relaxed until all forces were lower than 0.005 eV/Å, while for larger systems (surfaces and interfaces) the threshold was set to 0.05 eV/Å. Preliminary analysis on the polymorph stability (see Figure 1 and Table 1) confirms the experimental trend with the orthorhombic system as the most stable at room temperature, followed by the tetragonal, and the cubic.[51,52] This ordering has also been reported at the theoretical level,[53] further validating our setup. Following such results, we considered the orthorhombic polymorph for further surface/interface property analysis.[52]

To reveal the role of electron−hole interactions and local-field effects, the optical spectra were calculated using the Yambo code[54,55] based on preliminary self-consistent and nonself-consistent DFT calculations performed with the Quantum ESPRESSO suite.[56,57] Fully relativistic norm-conserving pseudopotentials (including spin−orbit coupling, SOC)[58] were employed, together with a kinetic-energy cutoff of 70 Ry and a shifted 6 × 6 × 6 k-point grid to converge the ground-state charge density. All calculations were performed using the PBE XC functional consistently with the previous calculations performed with VASP. Several studies have shown that an accurate description of the quasi-particle band structure of similar halide perovskites is highly sensitive to the underlying XC description and to nonharmonic lattice effects.[59−62] To avoid the well-known ambiguities related to the choice of the starting point in GW calculations of lead-free perovskites[63,64] considering the high-computational cost and, given the impact of anharmonicity[60,61]—we opted here not to perform GW simulations but to apply rigid scissor operators to

Table 1. PAW/PBE Calculated Structural Parameters (Lattice Constants and Volume), Energy Difference (ΔE) Relative to the Most Stable Polymorph, Formation Energy (E_{form}, eV) of the $Cs(Sn_{1-x}Ge_x)I_3$ Intermediate Alloys, and Energy Bandgap (E_{gap}, eV) of the Systems of Interest[a]

	$CsSnI_3$ Polymorph			$Cs(Sn_{1-x}Ge_x)I_3$ Alloys		$CsGeI_3$
	Cubic (α, $Pm3m$, Z = 1)	Tetragonal (β, $P_{4/mbm}$, Z = 2)	Orthorhombic (γ, $Pnma$, Z = 4)	x = 0.25	x = 0.50	Trigonal ($R3m$ Z = 1)
Lattice param. (Å)	a = 6.17 (a = 6.22)[52] (a = 6.13)[75]	a = 8.61; c = 6.26 (a = 8.77; c = 6.26)[52] (a = 8.61; c = 6.11)[75]	a = 8.82; b = 8.39; c = 12.36 (a = 8.69; b = 8.64; c = 12.38)[52] (a = 8.59; b = 8.54; c = 12.24)[75]	a = 8.66; b = 8.44; c = 12.09	a = 8.52; b = 8.43; c = 12.09	a = 5.93 (a = 5.98)[76] (a = 5.98)[34]
Vol. (Å^3)	234.54 (240.52,[52] 230.39[75])	463.77 (481.77,[52] 453.03[75])	915.27 (929.47,[52] 897.84[75])	892.64	869.08	208.55 (213.98)[34,76]
ΔE (eV/fu.)	+0.065	+0.02	0.0			
E_{form} (eV)				0.07	0.059	
E_{gap} (eV)			0.70	0.623	0.612	0.680

[a]Data in parentheses are from experiments (Z, formula unit per cell).

https://doi.org/10.1021/acsami.6c00873
ACS Appl. Mater. Interfaces 2026, 18, 32782−32794

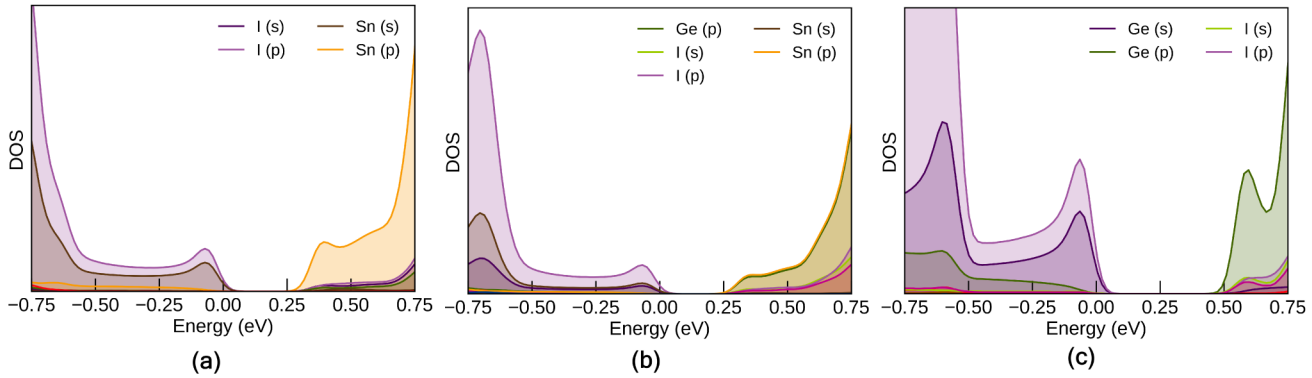

Figure 2. PAW/PBE + SOC-calculated Projected Density of States of (a) γ-$CsSnI_3$, (b) $Cs(Sn_{1-x}Ge_x)I_3$ (x = 0.50) alloyed system, and (c) $CsGeI_3$.

compensate the PBE + SOC gap underestimation and bring the first optical peak positions in agreement with the onset of the available experimental absorption data.[40,65−66] The scissor operator values turn out to be 1.25 eV for tin-based and 0.9 eV for germanium and the alloyed perovskite. Optical spectra were obtained by solving the Bethe-Salpeter Equation (BSE) considering an 8 × 8 × 6 (8 × 8 × 8 for the Ge-case) Γ centered k-grid and four valence and conduction states. Furthermore, we adopted the Tamm−Dancoff approximation, and the double-grid technique, as implemented in the Yambo code,[67] has been employed to speed up the convergence of the optical spectra with respect to the k-points grid.

Concerning surface termination, we selected the (001) orientation since, together with the (110) surface, it is reported to have lower cleavage energy in γ-$CsSnI_3$. This implies that the (001) surface is preferentially exposed and more prone to the formation of heterostructures with protection layers.[68] Accordingly, the (001) surface is selected in the following calculations to investigate the interfaces formed with GeO_2, both in its crystalline (r-GeO_2) and amorphous structure. Not secondarily, previous theoretical simulations focused on the same surface[53] providing data for comparison. GeO_2 is well known to exist both as quartz and rutile. While the former α-GeO_2 is metastable at ambient conditions,[69] the rutile polymorph represents the naturally occurring GeO_2 form.[70−72] Accordingly, in order to study $Cs(Sn_{1-x}Ge_x)I_3$−GeO_2 interfaces we focused our attention on rutile. Paying attention to the r-GeO_2 slab, the construction of such interfaces may be based on two different approaches. The first and the most common consists in keeping fixed the lateral parameters of the whole interface to those of the substrate. Within this framework, we found the (100) surface to provide the best lattice matching with the lateral parameter of $Cs(Sn_{1-x}Ge_x)I_3$ (x = 0.25). While such approach may better mimic the experimental growth conditions—and has been successfully applied in our previous theoretical investigations of several interfacial systems[73,74] at the same time tends to (over)localize the interfacial strain predominantly on a single component (in this case, GeO_2). This effect is further exacerbated when the simulation cell is minimized to limit computational cost. Consequently, we chose to share the total stress equally between the two components, thus applying tensile (compressive) stress on the $Cs(Sn_{1-x}Ge_x)I_3$ (r-GeO_2) component. Within this scheme, the best lattice match was obtained for the $Cs(Sn_{1-x}Ge_x)I_3$ (001) surface interfaced with the (001) surface of r-GeO_2. Further discussion of the interface assembly procedure is reported below. We first considered a 6-layer-thick rutile GeO_2 bulk consisting in 48 GeO_2 units to construct the initial crystalline interface. Following the 0 K optimization, to better mimic the experimental findings, we have assembled further interfaces with amorphous germania. To this end, we have expanded the germania volume (by ∼10%) breaking the symmetry of the initially optimized structure of the oxide supercell. A series of *ab initio* molecular dynamics (AIMD) simulations in the NVT canonical ensemble was then performed. The system was first thermalized at 4500 K for ∼25 ps (τ = 1.0 fs), and then quenched toward room temperature. The quenching procedure involved an initial relatively slow cooling rate (2.0×10^{14} K s^{-1}) followed, below 2500 K, by an increased cooling rate of 4.5×10^{14} K s^{-1}. The system obtained in this way was finally reoptimized at the DFT level. In all the interfaces here considered, a sufficient amount of vacuum is added along the nonperiodic direction in order to avoid any possible spurious interaction between replicas.

RESULTS AND DISCUSSION

Structural, Electronic, and Optical Properties of Perovskites

We initially calculated and reported in Table 1 the optimized lattice parameters of the three $CsSnI_3$ polymorphs, shown in Figure 1a−c along with the energies (ΔE) relative to the most stable $CsSnI_3$ polymorph, values that are in good agreement with previously reported theoretical[75] and experimental data.[51,52] In detail, the bulk orthorhombic $CsSnI_3$ structure is characterized by an Sn−I bond length of 3.13 Å, both along the apical and equatorial directions, with corresponding Sn−I−Sn bond angles of 160° and 152.2°, respectively. To complete the scenario, we also report the optimized structure $CsGeI_3$ (see Figure 1f), its structural parameters (still in Table 1) and the optimized structures of $Cs(Sn_{1-x}Ge_x)I_3$ (x = 0.25, 0.50) alloyed systems (see Figure 1d,e). Interestingly, we observe the experimentally reported pattern of two alternating Ge−I bond lengths, short (2.81 Å) and long (3.14 Å), a feature that will be particularly recursive also in the interfacial systems.

To create the (Sn,Ge)-alloyed systems, we first randomly substituted one Sn atom with a Ge atom in the bulk orthorhombic γ-$CsSnI_3$ unit cell (see Figure 1c) thereby obtaining $Cs(Sn_{1-x}Ge_x)I_3$ (x = 0.25, Figure 1d). This substitution induces an overall shrinkage of the volume of ∼2.3% (from 914.64 $Å^3$ in the pristine cell to 893.14 $Å^3$ in the final x = 0.25 Ge-alloyed one). Furthermore, as additional confirmation of the validity of our approach, we calculated the bandgap for γ-$CsSnI_3$, obtaining a value (@PBE/PAW level of theory) of 0.70 eV. Replacing 25% Sn with Ge, we obtain a

https://doi.org/10.1021/acsami.6c00873
ACS Appl. Mater. Interfaces 2026, 18, 32782−32794

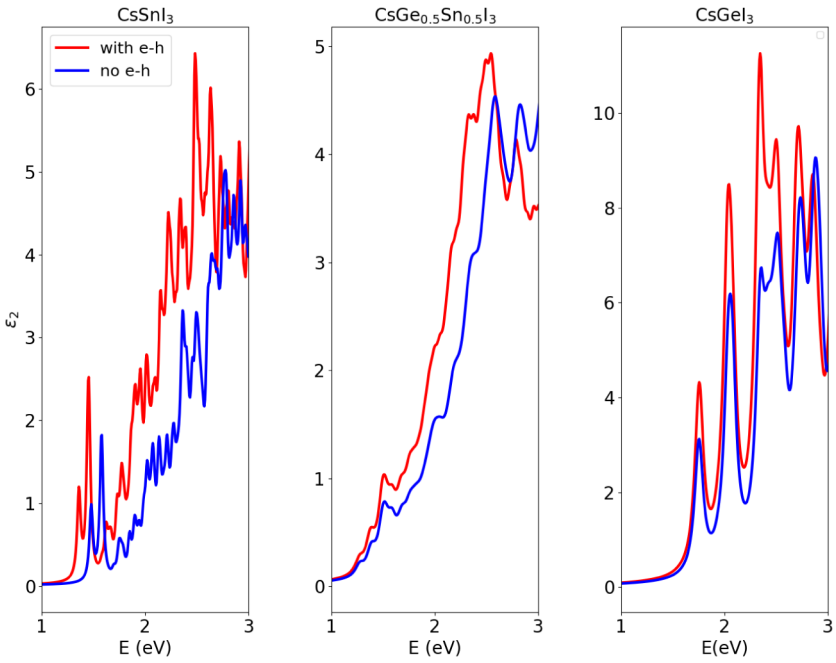

Figure 3. Optical spectra of the three different parent compounds, (left) orthorhombic γ-$CsSnI_3$, (middle) $CsSn_{0.5}Ge_{0.5}I_3$, and (right) rhombohedral $CsGeI_3$, calculated with and without electron−hole interaction.

modest but observable narrowing of the gap (0.63 eV), confirming the results of Chang et al.,[77] who report a progressive decrease of the alloy bandgap for $0 < x < 0.50$ and a symmetrical increase in the range $0.5 < x < 1.0$. The same trend is also observed when relativistic effects are included in the calculations. The electronic band structure calculated at the PBE + SOC level of approximation for the two pristine $CsSnI_3$ and $CsGeI_3$ systems along with that for the $Cs(Sn_{1-x}Ge_x)I_3$ ($x = 0.50$) alloy is reported in Figure S1 in the Supporting Information section. The corresponding PDOS, which are important for rationalizing the different roles of excitonic effects in the optical spectra, are reported in Figure 2.

To evaluate the relevance of the mixed alloy with respect to the pristine compounds, we computed and compared the optical spectra of $CsSnI_3$, $CsSn_{0.5}Ge_{0.5}I_3$, and $CsGeI_3$ (see Figure 3). The spectra were calculated both including (red solid lines) and neglecting (blue solid lines) excitonic and local-field effects. Our results show that the red shift and the enhancement of the main absorption peaks induced by electron−hole interactions are significant only in the Sn-based perovskite. In contrast, excitonic effects are much weaker in the Ge-containing compound and in the mixed alloy, whose spectra remain very close to the independent-particle ones. Due to the large dimensions of the BSE matrix, we employed the Haydock solver to obtain absorption spectra, though this approach precludes direct access to excitonic eigenvalues. Therefore, the exciton binding energies were estimated from the difference between the absorption onset calculated with and without electron−hole interactions (red and blue curves in Figure 3). This estimate yields a binding energy of approximately 100 meV for $CsSnI_3$, whereas values at least 1 order of magnitude smaller are obtained for the other two compounds. Therefore, the exciton binding energies were estimated from the difference between the absorption onset calculated with and without electron−hole interactions (red and blue curves in Figure 3). In this regard, it is important to emphasize that neither polaronic effects nor the ionic contribution to dielectric screening were included in the present work. As reported in the literature for some halide perovskites,[59,63,78] the inclusion of these effects is expected to enhance the overall screening and consequently reduce the calculated exciton binding energies, likely alleviating the discrepancy with ref 59. At the same time, these corrections are not expected to modify the qualitative trends identified in the present study, since our analysis considers only the electronic contribution to dielectric screening, treated consistently across all the systems investigated. The analysis of the projected density of states (PDOS, Figure 2) in the vicinity of the VBM and CBM provides a clear explanation of this behavior. In $CsSnI_3$, the states near the VBM (CBM) are dominated by the s (p) orbitals of Sn, which are highly hybridized with I p ones, whereas in (Sn,Ge)-mixed and Ge-pure systems, the VBM progressively acquires a dominant contribution from the p orbitals of I, while the CBM is primarily localized on the p orbitals of Ge (of both Ge and Sn in the (Sn,Ge)-mixed structure). This gradual change from an intra-atomic excitation character, dominated by $Sn(s) \rightarrow Sn(p)$ transition in $CsSnI_3$ to a predominantly interatomic character, namely $I(p) \rightarrow Sn(p)$, $Ge(p)$ transitions in the Ge-based and alloyed systems explains the observed reduction of excitonic effects. In such cases, the electron−hole interaction becomes less effective when the electron and hole are more spatially separated or reside on different atomic species.

From Bulk to Surface: Slab Thickness Convergence

Passing to the surface analysis, we check at first the slab thickness convergence of symmetric slabs vs the formation energy on the pristine γ-$CsSnI_3$ (001) surface, paying initial attention to the MI_2-terminated one. To take into account the nonstoichiometric nature of the slab we have to include another contribution that takes into account the excess of SnI_2 (which anyway is constant) following the equation:

https://doi.org/10.1021/acsami.6c00873
ACS Appl. Mater. Interfaces 2026, 18, 32782−32794

$$E_{form} = \frac{E_{slab}(11s) - (n \times \mu_{CsSnI_3} + 2 \times \mu_{SnI_2})}{2A} \quad (1)$$

Here, s in $E_{slab}(11s)$ is the number of bulk units along (001) direction with relative energy (E_{slab}). Each bulk unit contains two layers of perovskite along the (001) direction and s tested values are 2, 3, and 4, respectively (see Figure 1c). μ_{CsSnI_3} (and relative amount, n) and μ_{SnI_2} are the chemical potentials for $CsSnI_3$ (γ-$CsSnI_3$), and SnI_2 (space group 12, $C2/m$),[79] respectively. n values considered here are accordingly 8, 12, and 16, respectively. A is the in-plane surface area. After calculating E_{form} for s = 2, 3, 4 we observed a plateau (E_{form}= 0.26 J m^{-2}, s = 2; E_{form} = 0.28 J m^{-2}, s = 3; and E_{form} = 0.29 J m^{-2}, s = 4) and accordingly considered sufficient 3 units (6 layers) thick slabs for all the calculations, for both pristine γ-$CsSnI_3$ and γ-$Cs(Sn,Ge)I_3$ (001) surfaces. The slab thickness convergence test is followed by the calculation of the formation energy of the different terminations of the $Cs(Sn_{1-x}Ge_x)I_3$ (x = 0.25) (001)-oriented slabs. In particular, we observe how both terminations, namely CsI and MI_2 (M = Sn, Ge), prefer germanium to the outermost layer (in the former case, we mean the layer immediately below the CsI layer at the very surface). In particular, by looking at Figure 4, where all the optimized structures of the perovskite slabs are reported, for the MI_2 termination, the formation energy of the structure depicted in Figure 4b (M_2 = Ge only) is lower by 0.115 eV than that in Figure 4a (M_1 = Sn,Ge). For the CsI termination , the slab with a purely Ge layer immediately beneath the surface (M_2) is more stable than that containing a mixed $(Sn,Ge)I_2$ layer (still immediately beneath the surface) (M_1, Figure 4c) by 0.124 eV. This indicates a general tendency of Ge atoms to segregate toward the surface. In the following paragraph we describe the construction of the interface between each perovskite slab and germania, without further analyzing the relative thermodynamic stability of the slab models introduced above.

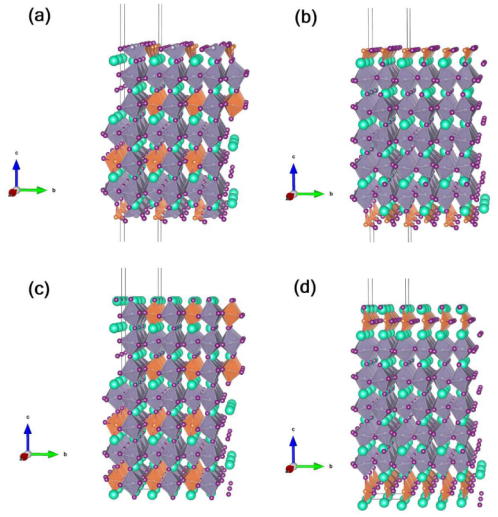

Figure 4. PAW/PBE-optimized structure of (a–b)MI_2-terminated and (c–d) CsI-terminated (001)-oriented slabs of γ-$Cs(Sn_{1-x}Ge_x)I_3$ (x=0.25). M = Ge only at the surface (GeI_2) in (b) and at the subsurface (CsI termination) in (d). Here, for the sake of visualization polyhedral representation is reported. [Mauve: Sn; Orange: Ge; Purple: I; Cyan: Cs atoms].

Interface Formation with GeO_2

We have successfully assembled and analyzed the interfaces formed between (1 × 1) $Cs(Sn_{1-x}Ge_x)I_3$ (001)-oriented surfaces and a (2 × 2) supercell of r-GeO_2, still (001)-oriented. When studying any interface, the primary consideration is the stress arising from the lattice mismatch between its components, as detailed in the Computational Details section. If we were to keep the lattice parameters of $Cs(Sn_{1-x}Ge_x)I_3$ fixed, the germania slab would experience extreme stress. This is because the PAW/PBE-optimized lattice parameters for its (2 × 2) supercell are a = b = 8.88 Å. To mitigate this issue, we applied a tensile stress to the bottom component and a compressive stress to the top component of the interface. This approach ensures that both $Cs(Sn_{1-x}Ge_x)I_3$ and r-GeO_2 experience a stress of ∼3.6% relative to their fully optimized counterparts. This level of stress is reasonable, as demonstrated in Figure 5, which compares the electronic characteristics of stressed versus relaxed structures for the two bulk systems. Notably, the electronic features (Density of States, DOS, and band structure/dispersion) are largely preserved also under these stressed conditions. Therefore, the lateral parameters used for all interfaces are a = 8.765 Å and b = 8.665 Å. Table 2 presents the main electronic features of the halide perovskite slabs involved in the interface formation. The four optimized interface structures formed with r-GeO_2 are shown in Figure 6.

Before we tackle the study of electronic properties, we focus on the structural analysis of the interfaces considered here. Let us begin with the CsI-terminated system with M = Sn, Ge (M_1) in the layer immediately below the surface (shown in Figure 6a). The characteristic structure of Ge halide perovskites is generated by three short bonds (2.83, 2.83, and 2.86 Å) and three long bonds (3.18, 3.28, and 3.32 Å), giving rise to the umbrella-like shape typical of such compounds,[34] as we previously discussed. When only germanium is present in the layer beneath the surface (M_2=Ge only, Figure 6b), we observe the same phenomenon reported. In this case, also, there are three long bonds (3.03, 3.41, and 3.57 Å) and three short ones (2.73, 2.82, and 2.95 Å). It is interesting to note that of the three long bonds, one is at the surface (3.03 Å), which causes a partial separation of the oxide from the perovskite. In fact, the germanium in the oxide layer forms a Ge–I bond at the interface of 2.84 Å, which is significantly shorter than the apical Ge–I bond discussed earlier: the iodine atoms at the surface tend to migrate from the perovskite, therefore passivating the oxide component.

Structurally, MI_2-terminated systems are of special interest. In detail, starting from the mixed composition (M_1=Sn,Ge), we observe how the coexistence of these two elements at the perovskite surface results in a particularly heterogeneous interface geometry (shown in Figure 6c). As in previous cases, Ge atoms at the terminating layer of the perovskite form three short bonds and three longer ones. With regard to the former, two bonds are formed between Ge and O (2.03 and 2.23 Å), while the third is formed between Ge and I (2.76 Å), the latter being a remnant of the initial perovskite structure. For the Sn atom, it forms up to six bonds, four with iodine (ranging from 2.48 to 3.52 Å) and two shorter ones with oxygen (2.17 and 2.25 Å, respectively), revealing the more marked ionic nature for such interface, as also witnessed by the two- and 3-fold coordinated I atoms at the interface.

The last investigated structure (reported in Figure 6 d) presents germanium atoms only at the surface of the perovskite

https://doi.org/10.1021/acsami.6c00873
ACS Appl. Mater. Interfaces 2026, 18, 32782–32794

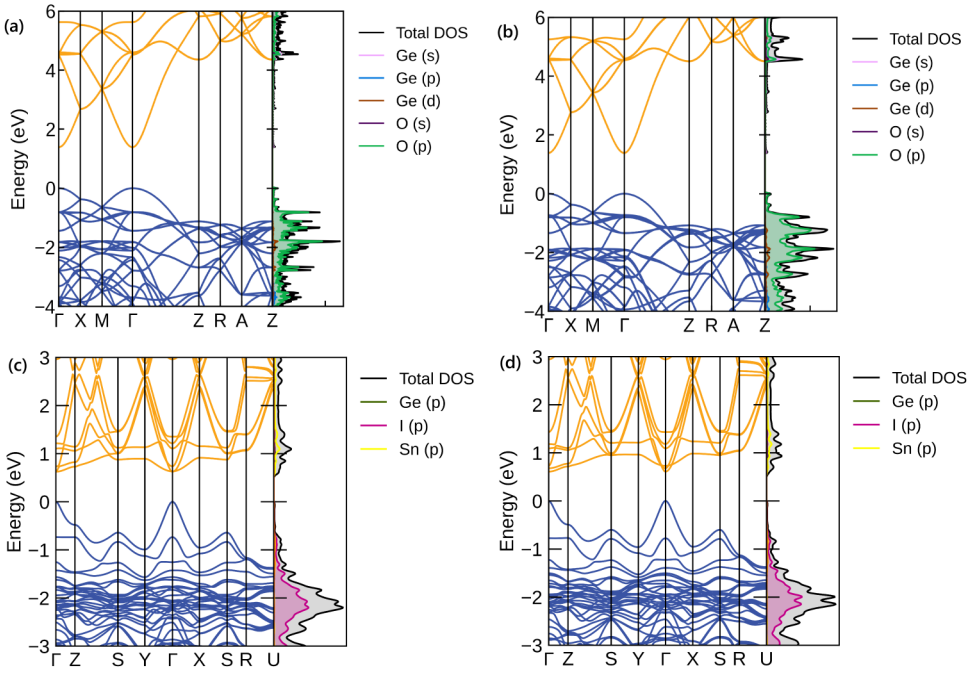

Figure 5. PAW/PBE-calculated band structure and DOS for (a) relaxed and (b) stressed (2 × 2) supercell of *r*-GeO_2. (c) and (d) are the same for the *γ*-$Cs(Sn_{1-x}Ge_x)I_3$ (x=0.25) unit cell.

Table 2. PAW/PBE Calculated Bandgap and Workfunction (Wf) for the Perovskite Slabs Here Considered[a]

	$CsSnI_3$	$Cs(Sn_{1-x}Ge_x)I_3$ (x = 0.25)				
	SnI_2-Term (Rel)	MI_2-Term (M_1=Sn,Ge) (Rel)	MI_2-Term (M_1=Sn,Ge) (Interf, **3**)	MI_2-Term (M_2=Ge) (Interf, **4**)	CsI-Term (M_1=Sn,Ge) (Interf, **1**)	CsI-Term (M_2=Ge) (Interf, **2**)
E_{gap} (eV)	0.86	0.81	0.73	0.83	0.74	0.54
Wf (Φ, eV)	5.02 (4.85)[80]	5.12	5.33	5.51	3.71	3.76

[a]"*rel*" refers to relaxed, no constraints systems; "*interf*" refers to values calculated keeping fixed the lateral parameters to those of the final interface. For CsI-terminated systems "M" refers to the first metal layer just immediately beneath the surface. In parenthesis is reported the experimental value for $CsSnI_3$.

(M_2 = Ge). The optimized structure reveals how the surface perovskite layer, here consisting of GeI_2, is completely detached from its pristine position and torn away by the oxide. In this configuration, the oxide saturates its surface layer, leaving the perovskite terminated with the subsuperficial SnI_2 layer.

A way to evaluate the stress at the interface is to consider the total stress energy defined as the difference between the total energies of the interface systems and the sum of the energies of the corresponding bulk GeO_2 and $Cs(Sn_{1-x}Ge_x)I_3$ phases. Although this approach is certainly valuable as it allows the calculation of both chemical and mechanical stress at the interface, it is probably more suitable and quantitative for periodic double-interface models,[81] where surface effects are minimized and, more importantly, no layers are kept frozen. In the present case, we evaluate the energetics of the system by calculating the adhesion energy, i.e., the opposite of the energy required to separate the surfaces that form the interface, as

$$E_{adh} = E_{interf} - (E_{Cs(Sn,Ge)I_3\text{-slab}} + E_{GeO_2\text{-slab}}) \quad (2)$$

where E_{interf} is the energy of the optimized interface, and $E_{Cs(Sn,Ge)I_3\text{-slab}}$ and $E_{GeO_2\text{-slab}}$ are the energies of the slab of $Cs(Sn_{1-x}Ge_x)I_3$ and of GeO_2, respectively. The results are reported in Table 3 and reveal that the MI_2-terminated slab tends to form more stabilized interfaces in both the case of pure Ge on the surface and in the mixed case.

For all the interfaces we have then calculated the electronic properties, i.e., DOS and valence band offset (VBO). Given the particularly large dimensions of our interface models, their electronic properties were evaluated only at the DFT level. It is well known that standard DFT functionals systematically underestimate excited-state properties, such as band gaps, due to their mean-field, ground-state nature. However, this limitation does not compromise the present analysis, as the underestimation is largely systematic and comparable across all the investigated systems. Consequently, relative trends and comparisons remain meaningful. For the calculation of VBO we have employed the formalism of van de Walle and Martin,[82] successfully applied to several other interfaces:[74]

$$\Delta\epsilon_{VBO} = (\epsilon_V^{Cs(Sn_{1-x}Ge_x)I_3} - \overline{V}_{bulk}^{Cs(Sn_{1-x}Ge_x)I_3}) - (\epsilon_V^{GeO_2} - \overline{V}_{bulk}^{GeO_2}) + \Delta\overline{\overline{V}} \quad (3)$$

where $\epsilon_V^{Cs(Sn_{1-x}Ge_x)I_3}$ and $\epsilon_V^{GeO_2}$ are the valence band maxima of $Cs(Sn_{1-x}Ge_x)I_3$ and GeO_2, respectively, while $\overline{V}_{bulk}^{Cs(Sn_{1-x}Ge_x)I_3}$ and $\overline{V}_{bulk}^{GeO_2}$ are the nanosmoothed averaged electrostatic potentials in $Cs(Sn_{1-x}Ge_x)I_3$ and GeO_2 slabs, respectively. $\Delta\overline{\overline{V}}$ is the difference between the nanosmoothed averaged

https://doi.org/10.1021/acsami.6c00873
ACS Appl. Mater. Interfaces 2026, 18, 32782−32794

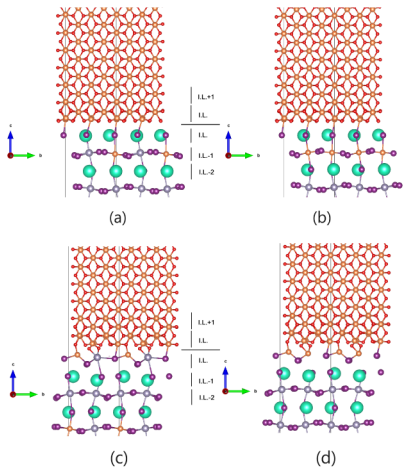

Figure 6. PAW/PBE-optimized structure of the four considered interfaces: CsI-terminated with (a) (Sn,Ge)-mixed layer beneath the perovskite surface layer (M_1, **1** in Table 3) (b) Ge only (M_2) (**2**); MI_2-terminated with (c) (Sn,Ge)-mixed termination (M_1) at the perovskite surface (**3**), (d) Ge only at the perovskite surface (M_2, **4**). For the sake of visualization a (2 × 2) supercell is reported. [Mauve: Sn; Orange: Ge; Purple: I; Red: O; Cyan: Cs atoms]. Figures (a) and (c) illustrate the layer-resolved breakdown of the interfaces used for PDOS analysis, projected onto individual layers (see Supplementary Figure S4).

Table 3. PAW/PBE Calculated Adhesion Energy and Bandgap of the Four Interfaces Here Investigated

Interface (Termination)	Adhesion Energy (eV, J m^{-2})	Bandgap (eV)
1 (CsI−, M_1=Sn,Ge)	−2.51 (−0.529)	0.49
2 (CsI−, M_2=Ge only)	−2.47 (−0.521)	0.39
3 (MI_2−, M_1=Sn,Ge))	−4.40 (−0.928)	(*metallic*)
4 (MI_2−, M_2=Ge only))	−4.67 (−0.985)	(*metallic*)

electrostatic potentials at the interface. We calculated a $\Delta\epsilon_{VBO}$ for the four interfaces, which ranges between 0.39 eV (interface **1**) and 1.69 eV (interface **4**), revealing the completely different nature of the interfaces as a function of the perovskite termination. The planar averaged electrostatic potential for the four interfaces here investigated is reported in Figure S2 in Supporting Information. We additionally show the DOS for the four interfaces in Figure 7, along with the Projected Density of States onto the different layers at the interfaces (see Figure S4 in Supporting Information).

While the two CsI-terminated interfaces are characterized by a bandgap, both MI_2-terminated interfaces are metallic. This finding is consistent with previously reported data—mostly ascribed to strain-induced effects—for interfaces between silicon and methylammonium lead iodide ($MAPbI_3$), where analogous termination-dependent behavior was observed: PbI_2-terminated interfaces are metallic, whereas the MAI-terminated ones are characterized by a bandgap.[74] To gain further insight, we analyzed the squared modulus of the band-edge wave functions for the CsI-terminated interfaces The first investigated interface (**1**) has a VBM mainly constituted by I 5*p* orbitals (61%), by Sn 5*s* orbitals (34.5%), and by Ge 4*s* ones (∼4.0%), the latter belonging to the perovskite slab. The CBM is at variance constituted by 61% of Ge 4*s* orbitals and ∼28% of O 2*p*, these two latter belonging to the GeO_2 slab and mostly localized at the interface. Similar behavior is observed for the second interface (**2**) where the VBM is located mainly in the inner region of the perovskite and the CBM in the GeO_2 layer forming the interface. The overall picture that emerges from this orbital (de)localization is that the interface region acts as a recombination center, due to the extremely localized nature of the electrons at the interface.

To complete the picture, we establish a parallelism between crystalline and amorphous germania and their influence on the electronic features of the interfaces under investigation. We used the same perovskite slabs, onto which we placed the amorphous germania constructed following the procedure described in the Computational Details section. As a result, we obtain three stable interfaces (those formed with MI_2-terminated (M_1 = Sn, Ge) are thermodynamically unstable), whose structures are reported in Figure 8 and whose adhesion energies are reported in Table 4. The values—clearly more exothermic than those of the crystal−crystal counterparts—reflect the enhanced formability of the amorphous-crystalline interfaces because of the disordered amorphous structure and the lack of a long-range order. These results similarly highlight the larger tolerance and flexibility of the amorphous phase when interacting with the more-ordered atomic framework of the crystalline perovskite slab.

The modulus of the VBM and CBM wave functions provides a direct, microscopic visualization of the real-space localization of the frontier orbitals at the interface, which is a widely accepted indicator of charge transfer propensity and chemical reactivity in DFT studies of heterostructures.[74,83,84] The most relevant outcome of our analysis is the completely different behavior of the band edge states at the interfaces involving amorphous versus crystalline GeO_2. For the latter (as shown in Figure 9), we observed that the interfaces act as recombination centers, while the amorphous germania interfaced with the (Sn, Ge)-alloyed perovskite shows an opposite trend. The VBM is indeed localized in the germania, corresponding to an enhanced localization of electrons in such a region, as shown in Figure 10. This means that amorphous oxide tends to preserve the perovskite layer and prevent its eventual oxidation, a result that supports previous experimental works[40] that clearly claim the beneficial effect in terms of stability of an amorphous oxide layer on top of mixed-halide (Sn,Ge) perovskites. Before concluding, we should spend a few words of caution regarding our findings for both crystalline and amorphous oxide systems. While we observe that adhesion energies clearly favor MI_2-terminated $Cs(Sn,Ge)I_3/GeO_2$ interfaces, the resulting metallic character (small/no-gap states) and large VBO (in the crystalline case) arise from static DFT-PBE models of reactive crystal/crystal contacts, where optimization induces GeI_2-like species akin to PbI_2 formation under atomic layer-deposited SnO_2[85] and dangling bonds from rigid MI_2 terminations.[74] Amorphous GeO_2 cases, modeled following the experimentally reported procedure,[40] retain residual strain from lattice averaging, likely exaggerating gap states versus dynamic deposition. Prepassivation of the oxide electron transport layer[86] would definitely mitigate recombination risks and band misalignment in devices. Not secondarily, the level of theory we employed is by construction unable to capture the exact nature of the bandgap (mostly for what concerns the excited-state properties). On the other hand, more accurate methods such as HSE06 hybrids or GW are computationally prohibitive for our large supercells due to their relevant scaling with system size.

https://doi.org/10.1021/acsami.6c00873
ACS Appl. Mater. Interfaces 2026, 18, 32782−32794

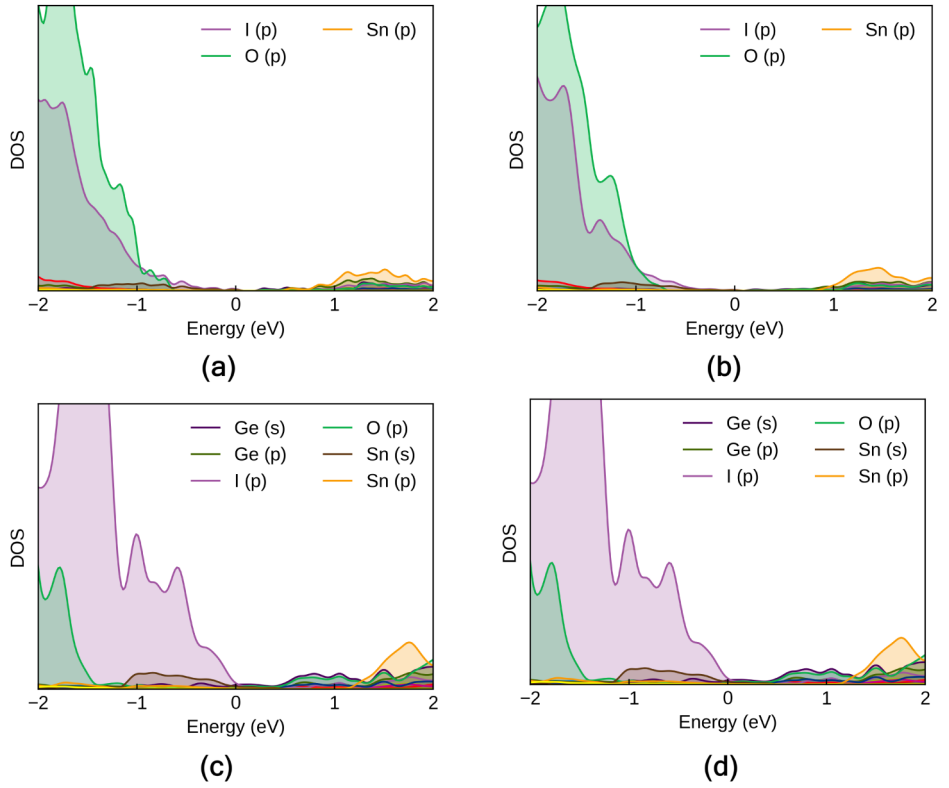

Figure 7. Total and Projected Density of States for the four interfaces formed by crystalline *r*-GeO_2 and $Cs(Sn_{1-x}Ge_x)I_3$ (x = 0.25). CsI-terminated with (a) mixed (Sn, Ge) layer beneath the perovskite surface (M_1, **1** in Table 3) (b) Ge only in the layer beneath the perovskite surface (M_2, **2**); MI_2-terminated with (c) mixed (Sn, Ge) at the perovskite surface (M_1, **3**), (d) Ge only at the perovskite surface (M_2, **4**).

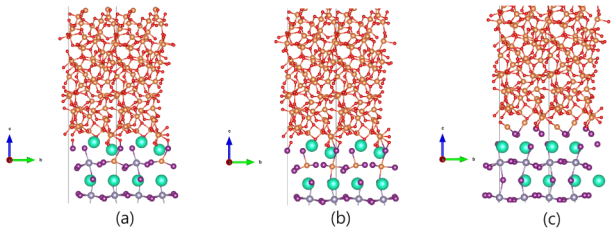

Figure 8. PAW/PBE-optimized structure of the four interfaces formed by amorphous germania here considered: CsI-terminated with (a) mixed (Sn, Ge) layer beneath the perovskite surface; (b) Ge only layer beneath the perovskite surface; (c) MI_2-terminated with Ge only at the perovskite surface. For the sake of visualization a (2 × 2) supercell is reported. [Mauve: Sn; Orange: Ge; Purple: I; Red: O; Cyan: Cs atoms].

Table 4. PAW/PBE Calculated Adhesion Energy and Bandgap of the Investigated Three Stable Interfaces with Amorphous GeO_2

Interface (Termination)	Adhesion Energy (eV, J m^{-2})	Bandgap (eV)
1a (CsI−, M_1=Sn,Ge)	−5.76 (−1.214)	(*metallic*)
2a (CsI−, M_2=Ge only)	−6.86 (−1.446)	0.013
4a (MI_2−, M_2=Ge only)	−7.74 (−1.631)	0.007

CONCLUSIONS

Given the technological relevance of lead-free halide perovskites, we have investigated interfaces between oxides and lead-free (Sn,Ge)-mixed halide perovskites. We have at first considered the three perovskite parental compounds, i.e., $CsSnI_3$ and $CsGeI_3$, and their alloyed system $Cs(Sn_{1-x}Ge_x)I_3$.

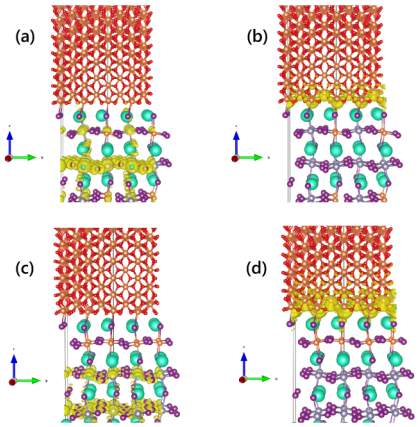

Figure 9. (a) Valence Band Maximum and (b) Conduction Band Maximum wave function square modulus for the **1** interface. (c) and (d) are the same for the **2** interface. For the sake of visualization a (2 × 2) supercell is reported. [Mauve: Sn; Orange: Ge; Purple: I; Red: O; Cyan: Cs atoms] (isosurface level 3 × 10^{-4} e/Bohr^{-3}).

The comparison of their optical spectra demonstrates that pronounced excitonic red shifts and intensity enhancements are a distinctive feature of $CsSnI_3$ only, whereas excitonic effects remain weak in the Ge-based and mixed systems, whose responses closely follow the independent-particle behavior. Markedly different behavior is observed studying amorphous and crystalline germania when interfaced with $Cs(Sn_{1-x}Ge_x)I_3$. We both considered MI_2- (M_1=Sn,Ge; M_2=Ge only) and CsI-(M_1=Sn,Ge; M_2=Ge only at the layer immediately under the CsI outmost layer) terminated perovskites and observed that the former form more stable interfaces (more exothermic

https://doi.org/10.1021/acsami.6c00873
ACS Appl. Mater. Interfaces 2026, 18, 32782−32794

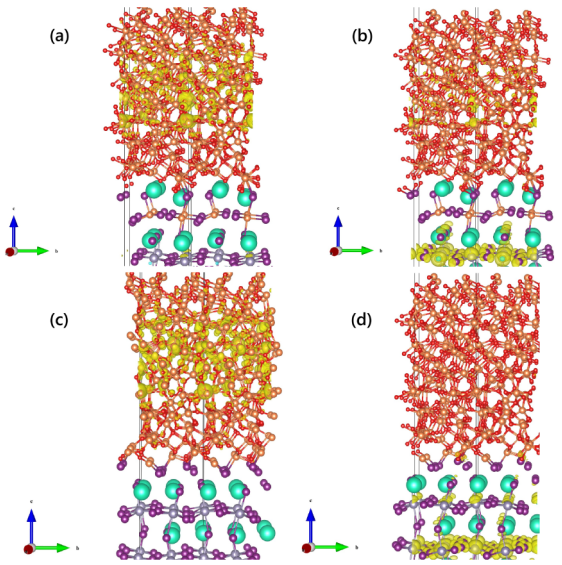

Figure 10. (a) Valence Band Maximum and (b) Conduction Band Maximum Wave function square modulus for the **2a** interface. (c) and (d) are the same for the **4a** interface. For the sake of visualization a (2 × 2) supercell is reported. [Mauve: Sn; Orange: Ge; Purple: I; Red: O; Cyan: Cs atoms] (isosurface level 3×10^{-4} e/Bohr^{-3}).

adhesion energy) with r-GeO_2 compared to the latter ones. Both MI_2-terminated perovskite crystalline interfaces show a metallic character, while both considered CsI-terminated perovskite interfaces maintain a gap.

For interfaces with crystalline rutile GeO_2, the charge transfer is from the valence band maximum localized in the $Cs(Sn_{1-x}Ge_x)I_3$ perovskite, to the conduction band minimum, which is localized in the oxide part at the very interface. When the surface of the perovskite is terminated with GeI_2, such termination tends to drift toward GeO_2, providing an interesting structural characteristic common in both crystalline and amorphous systems (iodine passivation of the GeO_2 layer). For interfaces formed with amorphous GeO_2, the electronic characteristics are more heterogeneous compared to the case of crystalline rutile GeO_2: the interfaces with a bandgap are indeed those formed either with CsI- or GeI_2-terminated perovskite. For interfaces with amorphous GeO_2, charge transfer clearly takes place between the amorphous germania inner region (valence band maximum) and the perovskite inner region (conduction band minimum). This latter result is in fair agreement with experiments that reveal the benign formation of an oxide amorphous layer on top of the (Sn, Ge)-mixed perovskite. Such a layer is found to protect the perovskite slab and to prevent its oxidation, as clearly confirmed from our calculations.

■ ASSOCIATED CONTENT

Supporting Information

The Supporting Information is available free of charge at https://pubs.acs.org/doi/10.1021/acsami.6c00873.

PBE + SOC-calculated band structures for bulk perovskite systems; electrostatic potential profiles across the interfaces between the perovskite and crystalline r-GeO_2; surface formation energies and workfunctions of the perovskite terminations; density of states (DOS) of Ge atoms in the perovskite slabs closest to the interface formed with r-GeO_2; layer-by-layer contribution to the projected density of states (PDOS) at the perovskite/crystalline r-GeO_2 interface (PDF)

■ AUTHOR INFORMATION

Corresponding Authors

Maurizia Palummo − *Department of Physics & INFN, Universitá di Roma "Tor Vergata,", Roma 00133, Italy; Centro S3, CNR-Istituto Nanoscienze, Modena 41125, Italy;* orcid.org/0000-0002-3097-8523; Phone: +39-06-72594538; Email: maurizia.palummo@roma2.infn.it

Giacomo Giorgi − *Department of Civil & Environmental Engineering (DICA), The University of Perugia, Perugia 06125, Italy; CIRIAF - Interuniversity Research Centre, University of Perugia, Perugia 06125, Italy; Centro S3, CNR-Istituto Nanoscienze, Modena 41125, Italy; CNR-SCITEC, Perugia 06123, Italy;* orcid.org/0000-0003-4892-7908; Phone: +39-075-5853836; Email: giacomo.giorgi@unipg.it

Authors

Costanza Borghesi − *Centro S3, CNR-Istituto Nanoscienze, Modena 41125, Italy; Department of Civil & Environmental Engineering (DICA), The University of Perugia, Perugia 06125, Italy; CIRIAF - Interuniversity Research Centre, University of Perugia, Perugia 06125, Italy*

Azusa Muraoka − *Graduate School of Science, Japan Women's University, Tokyo 112-8681, Japan;* orcid.org/0000-0001-8005-0478

Suraya Shaban − *i-PERC, the University of Electro-Communications, Chofu, Tokyo 182-8585, Japan*

Shuzi Hayase − *i-PERC, the University of Electro-Communications, Chofu, Tokyo 182-8585, Japan;* orcid.org/0000-0001-8192-5336

Daniele Varsano − *Centro S3, CNR-Istituto Nanoscienze, Modena 41125, Italy;* orcid.org/0000-0001-7675-7374

Koichi Yamashita − *Graduate School of Nanobioscience, Yokohama City University, Yokohama 236-0027, Japan;* orcid.org/0000-0002-6226-3194

Complete contact information is available at: https://pubs.acs.org/10.1021/acsami.6c00873

Notes

The authors declare no competing financial interest.

■ ACKNOWLEDGMENTS

Authors acknowledge the Hanami (Hpc AlliaNce for Applications and supercoMputing Innovation: the Europe-Japan collaboration) project via the European High Performance Computing Joint Undertaking (EuroHPC JU) under the European Union's Horizon Europe framework program for research and innovation and Grant Agreement No. 101136269. The views and opinions expressed are those of the author(s) only and do not necessarily reflect those of the European Union or EuroHPC Joint Undertaking. Neither the European Union nor the granting authority can be held responsible. Authors acknowledge the NEDO Project of Research and Development Program for Promoting Innovative Clean Energy Technologies Through International Collaboration ("Development of materials for Pb free perovskite tandem solar cells"). M.P. acknowledges the PRIN Project 2022WL9MLA ("Hybrid pErovskite nanowiRes for OptoElectronic applicationS"), supported by the Next Generation EU program in the context

of the PNRR Italian plan, mission 4 "education and research". K.Y. acknowledges the support by MEXT as "Program for Promoting Research on the Supercomputer Fugaku" (Realization of innovative light energy conversion materials utilizing the supercomputer Fugaku, Grant No. JPMXP1020210317). G.G., D.V., and C.B. acknowledge the use of computational resources of the Fugaku Supercomputer provided under the General Access program (Project ID: hp250100).

REFERENCES

(1) Snaith, H. J. Perovskites: the emergence of a new era for low-cost, high-efficiency solar cells. *J. Phys. Chem. Lett.* **2013**, *4*, 3623−3630.
(2) Kojima, A.; Teshima, K.; Shirai, Y.; Miyasaka, T. Organometal halide perovskites as visible-light sensitizers for photovoltaic cells. *J. Am. Chem. Soc.* **2009**, *131*, 6050−6051.
(3) *NREL, Best Research-Cell Efficiencies*. https://www.nrel.gov/pv/cell-efficiency.html. (accessed Jan 2023).
(4) Kim, H.-S.; Lee, C.-R.; Im, J.-H.; Lee, K.-B.; Moehl, T.; Marchioro, A.; Moon, S.-J.; Humphry-Baker, R.; Yum, J.-H.; Moser, J. E.; et al. Lead iodide perovskite sensitized all-solid-state submicron thin film mesoscopic solar cell with efficiency exceeding 9%. *Sci. Rep.* **2012**, *2*, 591.
(5) Stranks, S. D.; Eperon, G. E.; Grancini, G.; Menelaou, C.; Alcocer, M. J.; Leijtens, T.; Herz, L. M.; Petrozza, A.; Snaith, H. J. Electron-hole diffusion lengths exceeding 1 micrometer in an organometal trihalide perovskite absorber. *Science* **2013**, *342*, 341−344.
(6) Giorgi, G.; Fujisawa, J.-I.; Segawa, H.; Yamashita, K. Small photocarrier effective masses featuring ambipolar transport in methylammonium lead iodide perovskite: a density functional analysis. *J. Phys. Chem. Lett.* **2013**, *4*, 4213−4216.
(7) Xing, G.; Mathews, N.; Sun, S.; Lim, S. S.; Lam, Y. M.; Grätzel, M.; Mhaisalkar, S.; Sum, T. C. Long-range balanced electron-and hole-transport lengths in organic-inorganic $CH_3NH_3PbI_3$. *Science* **2013**, *342*, 344−347.
(8) Brenner, T. M.; Egger, D. A.; Kronik, L.; Hodes, G.; Cahen, D. Hybrid organic—inorganic perovskites: low-cost semiconductors with intriguing charge-transport properties. *Nat. Rev. Mater.* **2016**, *1*, 15007.
(9) Mosconi, E.; Amat, A.; Nazeeruddin, M. K.; Gratzel, M.; De Angelis, F. First-principles modeling of mixed halide organometal perovskites for photovoltaic applications. *J. Phys. Chem. C* **2013**, *117*, 13902−13913.
(10) Stoumpos, C. C.; Malliakas, C. D.; Kanatzidis, M. G. Semiconducting tin and lead iodide perovskites with organic cations: phase transitions, high mobilities, and near-infrared photoluminescent properties. *Inorg. Chem.* **2013**, *52*, 9019−9038.
(11) Smith, I. C.; Hoke, E. T.; Solis-Ibarra, D.; McGehee, M. D.; Karunadasa, H. I. A layered hybrid perovskite solar-cell absorber with enhanced moisture stability. *Angew. Chem., Int. Ed.* **2014**, *53*, 11232−11235.
(12) Tsai, H.; Nie, W.; Blancon, J.-C.; Stoumpos, C. C.; Asadpour, R.; Harutyunyan, B.; Neukirch, A. J.; Verduzco, R.; Crochet, J. J.; Tretiak, S.; et al. High-efficiency two-dimensional Ruddlesden−Popper perovskite solar cells. *Nature* **2016**, *536*, 312−316.
(13) Cao, D. H.; Stoumpos, C. C.; Farha, O. K.; Hupp, J. T.; Kanatzidis, M. G. 2D homologous perovskites as light-absorbing materials for solar cell applications. *J. Am. Chem. Soc.* **2015**, *137*, 7843−7850.
(14) Stoumpos, C. C.; Cao, D. H.; Clark, D. J.; Young, J.; Rondinelli, J. M.; Jang, J. I.; Hupp, J. T.; Kanatzidis, M. G. Ruddlesden−Popper hybrid lead iodide perovskite 2D homologous semiconductors. *Chem. Mater.* **2016**, *28*, 2852−2867.
(15) Wang, F.; Jiang, X.; Chen, H.; Shang, Y.; Liu, H.; Wei, J.; Zhou, W.; He, H.; Liu, W.; Ning, Z. 2D-quasi-2D-3D hierarchy structure for tin perovskite solar cells with enhanced efficiency and stability. *Joule* **2018**, *2*, 2732−2743.
(16) Du, K.-Z.; Tu, Q.; Zhang, X.; Han, Q.; Liu, J.; Zauscher, S.; Mitzi, D. B. Two-dimensional lead (II) halide-based hybrid perovskites templated by acene alkylamines: crystal structures, optical properties, and piezoelectricity. *Inorg. Chem.* **2017**, *56*, 9291−9302.
(17) Giorgi, G.; Yamashita, K.; Palummo, M. Nature of the electronic and optical excitations of Ruddlesden−Popper hybrid organic−inorganic perovskites: The role of the many-body interactions. *J. Phys. Chem. Lett.* **2018**, *9*, 5891−5896.
(18) Quarti, C.; Giorgi, G.; Katan, C.; Even, J.; Palummo, M. Exciton ground state fine structure and excited states landscape in layered halide perovskites from combined BSE simulations and symmetry analysis. *Adv. Opt. Mater.* **2024**, *12*, 2202801.
(19) Folpini, G.; Palummo, M.; Cortecchia, D.; Moretti, L.; Cerullo, G.; Petrozza, A.; Giorgi, G.; Kandada, A. R. S. Plurality of excitons in Ruddlesden−Popper metal halides and the role of the B-site metal cation. *Mater. Adv.* **2023**, *4*, 1720−1730.
(20) Zhang, Y.; Park, N.-G. Quasi-two-dimensional perovskite solar cells with efficiency exceeding 22%. *ACS Energy Lett.* **2022**, *7*, 757−765.
(21) Jang, Y.-W.; Lee, S.; Yeom, K. M.; Jeong, K.; Choi, K.; Choi, M.; Noh, J. H. Intact 2D/3D halide junction perovskite solar cells via solid-phase in-plane growth. *Nature Energy* **2021**, *6*, 63−71.
(22) Ogomi, Y.; Morita, A.; Tsukamoto, S.; Saitho, T.; Fujikawa, N.; Shen, Q.; Toyoda, T.; Yoshino, K.; Pandey, S. S.; Ma, T.; et al. $CH_3NH_3Sn_xPb_{(1-x)}I_3$ Perovskite solar cells covering up to 1060 nm. *J. Phys. Chem. Lett.* **2014**, *5*, 1004−1011.
(23) Kapil, G.; Ripolles, T. S.; Hamada, K.; Ogomi, Y.; Bessho, T.; Kinoshita, T.; Chantana, J.; Yoshino, K.; Shen, Q.; Toyoda, T.; et al. Highly efficient 17.6% tin−lead mixed perovskite solar cells realized through spike structure. *Nano Lett.* **2018**, *18*, 3600−3607.
(24) Volonakis, G.; Filip, M. R.; Haghighirad, A. A.; Sakai, N.; Wenger, B.; Snaith, H. J.; Giustino, F. Lead-free halide double perovskites via heterovalent substitution of noble metals. *J. Phys. Chem. Lett.* **2016**, *7*, 1254−1259.
(25) Volonakis, G.; Haghighirad, A. A.; Milot, R. L.; Sio, W. H.; Filip, M. R.; Wenger, B.; Johnston, M. B.; Herz, L. M.; Snaith, H. J.; Giustino, F. $Cs_2InAgCl_6$: a new lead-free halide double perovskite with direct band gap. *J. Phys. Chem. Lett.* **2017**, *8*, 772−778.
(26) Igbari, F.; Wang, R.; Wang, Z.-K.; Ma, X.-J.; Wang, Q.; Wang, K.-L.; Zhang, Y.; Liao, L.-S.; Yang, Y. Composition stoichiometry of $Cs_2AgBiBr_6$ films for highly efficient lead-free perovskite solar cells. *Nano Lett.* **2019**, *19*, 2066−2073.
(27) Slavney, A. H.; Hu, T.; Lindenberg, A. M.; Karunadasa, H. I. A bismuth-halide double perovskite with long carrier recombination lifetime for photovoltaic applications. *J. Am. Chem. Soc.* **2016**, *138*, 2138−2141.
(28) McClure, E. T.; Ball, M. R.; Windl, W.; Woodward, P. M. Cs_2AgBiX_6 (X= Br, Cl): new visible light absorbing, lead-free halide perovskite semiconductors. *Chem. Mater.* **2016**, *28*, 1348−1354.
(29) Palummo, M.; Berrios, E.; Varsano, D.; Giorgi, G. Optical properties of lead-free double perovskites by ab initio excited-state methods. *ACS Energy Lett.* **2020**, *5*, 457−463.
(30) Savory, C. N.; Walsh, A.; Scanlon, D. O. Can Pb-free halide double perovskites support high-efficiency solar cells? *ACS Energy Lett.* **2016**, *1*, 949−955.
(31) Giorgi, G.; Yamashita, K.; Palummo, M. Two-dimensional optical excitations in the mixed-valence $Cs_2Au_2I_6$ fully inorganic double perovskite. *J. Mater. Chem. C* **2018**, *6*, 10197−10201.
(32) Palummo, M.; Varsano, D.; Berríos, E.; Yamashita, K.; Giorgi, G. Halide Pb-free double−perovskites: Ternary *vs*.quaternary stoichiometry. *Energies* **2020**, *13*, 3516.
(33) Azizman, M. S. A.; Azhari, A. W.; Halin, D. S. C.; Ibrahim, N.; Sepeai, S.; Ludin, N. A.; Nor, M. N. M.; Ho, L. N. Progress in tin-germanium perovskite solar cells: A review. *Synth. Met.* **2023**, *299*, 117475.
(34) Stoumpos, C. C.; Frazer, L.; Clark, D. J.; Kim, Y. S.; Rhim, S. H.; Freeman, A. J.; Ketterson, J. B.; Jang, J. I.; Kanatzidis, M. G. Hybrid germanium iodide perovskite semiconductors: active lone pairs, structural distortions, direct and indirect energy gaps, and

https://doi.org/10.1021/acsami.6c00873
ACS Appl. Mater. Interfaces 2026, 18, 32782−32794

strong nonlinear optical properties. *J. Am. Chem. Soc.* **2015**, *137*, 6804−6819.
(35) Dong, Y.; Zhao, Y.; Zhang, S.; Dai, Y.; Liu, L.; Li, Y.; Chen, Q. Recent advances toward practical use of halide perovskite nanocrystals. *J. Mater. Chem. A* **2018**, *6*, 21729−21746.
(36) Ito, N.; Kamarudin, M. A.; Hirotani, D.; Zhang, Y.; Shen, Q.; Ogomi, Y.; Iikubo, S.; Minemoto, T.; Yoshino, K.; Hayase, S. Mixed Sn−Ge perovskite for enhanced perovskite solar cell performance in air. *J. Phys. Chem. Lett.* **2018**, *9*, 1682−1688.
(37) Ng, C. H.; Nishimura, K.; Ito, N.; Hamada, K.; Hirotani, D.; Wang, Z.; Yang, F.; Likubo, S.; Shen, Q.; Yoshino, K.; et al. Role of GeI_2 and SnF_2 additives for SnGe perovskite solar cells. *Nano Energy* **2019**, *58*, 130−137.
(38) Hamada, K.; Kamarudin, M. A.; Zhen, W.; Hirotani, D.; Shen, Q.; Iikubo, S.; Minemoto, T.; Yoshino, K.; Toyoda, T.; Hayase, S. The effect of transparent conductive oxide substrate on the efficiency of SnGe-perovskite solar cells. *J. Photopolym. Sci. Technol.* **2019**, *32*, 597−602.
(39) Zhou, Y.-Q.; Xu, J.; Liu, J.-B.; Liu, B.-X. Alloy engineering in mixed Sn−Ge perovskites for photovoltaic application. *J. Mater. Chem. A* **2021**, *9*, 6955−6961.
(40) Chen, M.; Ju, M.-G.; Garces, H. F.; Carl, A. D.; Ono, L. K.; Hawash, Z.; Zhang, Y.; Shen, T.; Qi, Y.; Grimm, R. L.; et al. Highly stable and efficient all-inorganic lead-free perovskite solar cells with native-oxide passivation. *Nat. Commun.* **2019**, *10*, 16.
(41) Xi, J.; Loi, M. A. The fascinating properties of tin-alloyed halide perovskites. *ACS Energy Lett.* **2021**, *6*, 1803−1810.
(42) Kresse, G.; Furthmüller, J. Efficient iterative schemes for ab initio total-energy calculations using a plane-wave basis set. *Phys. Rev. B* **1996**, *54*, 11169.
(43) Kresse, G.; Furthmüller, J. Efficiency of ab-initio total energy calculations for metals and semiconductors using a plane-wave basis set. *Comput. Mater. Sci.* **1996**, *6*, 15−50.
(44) Kresse, G.; Hafner, J. Ab initio molecular-dynamics simulation of the liquid-metal−amorphous-semiconductor transition in germanium. *Phys. Rev. B* **1994**, *49*, 14251.
(45) Kresse, G.; Hafner, J. Ab initio molecular dynamics for open-shell transition metals. *Phys. Rev. B* **1993**, *48*, 13115.
(46) Perdew, J. P.; Burke, K.; Ernzerhof, M. Generalized gradient approximation made simple. *Phys. Rev. Lett.* **1996**, *77*, 3865.
(47) Blöchl, P. E. Projector augmented-wave method. *Phys. Rev. B* **1994**, *50*, 17953.
(48) Kresse, G.; Joubert, D. From ultrasoft pseudopotentials to the projector augmented-wave method. *Phys. Rev. B* **1999**, *59*, 1758.
(49) Grimme, S.; Antony, J.; Ehrlich, S.; Krieg, H. A consistent and accurate ab initio parametrization of density functional dispersion correction (DFT-D) for the 94 elements H-Pu. *J. Chem. Phys.* **2010**, *132*, 154104.
(50) Grimme, S.; Ehrlich, S.; Goerigk, L. Effect of the damping function in dispersion corrected density functional theory. *J. Comput. Chem.* **2011**, *32*, 1456−1465.
(51) Chung, I.; Song, J.-H.; Im, J.; Androulakis, J.; Malliakas, C. D.; Li, H.; Freeman, A. J.; Kenney, J. T.; Kanatzidis, M. G. $CsSnI_3$: semiconductor or metal? High electrical conductivity and strong near-infrared photoluminescence from a single material. High hole mobility and phase-transitions. *J. Am. Chem. Soc.* **2012**, *134*, 8579−8587.
(52) Yamada, K.; Funabiki, S.; Horimoto, H.; Matsui, T.; Okuda, T.; Ichiba, S. Structural phase transitions of the polymorphs of $CsSnI_3$ by means of rietveld analysis of the X-ray diffraction. *Chem. Lett.* **1991**, *20*, 801−804.
(53) Li, W.; Liu, P.; Wang, F.; Pan, L.; Guo, H.; Chen, Y.; Yang, S.-E. Phase stability and impact of water on $CsSnI_3$ perovskite. *Appl. Phys. Express* **2020**, *13*, 071003.
(54) Marini, A.; Hogan, C.; Grüning, M.; Varsano, D. Yambo: an ab initio tool for excited state calculations. *Comput. Phys. Commun.* **2009**, *180*, 1392−1403.
(55) Sangalli, D.; Ferretti, A.; Miranda, H.; Attaccalite, C.; Marri, I.; Cannuccia, E.; Melo, P.; Marsili, M.; Paleari, F.; Marrazzo, A.; et al. Many-body perturbation theory calculations using the yambo code. *J. Phys.: Condens. Matter* **2019**, *31*, 325902.
(56) Giannozzi, P.; et al. QUANTUM ESPRESSO: a modular and open-source software project for quantum simulations of materials. *J. Phys.: Condens. Matter* **2009**, *21*, 395502.
(57) Giannozzi, P.; et al. Advanced capabilities for materials modelling with QUANTUM ESPRESSO. *J. Phys.: Condens. Matter* **2017**, *29*, 465901.
(58) Van Setten, M. J.; Giantomassi, M.; Bousquet, E.; Verstraete, M. J.; Hamann, D. R.; Gonze, X.; Rignanese, G.-M. The PseudoDojo: Training and grading a 85 element optimized norm-conserving pseudopotential table. *Comput. Phys. Commun.* **2018**, *226*, 39−54.
(59) Huang, L.-Y.; Lambrecht, W. R. Electronic band structure, phonons, and exciton binding energies of halide perovskites $CsSnCl_3$, $CsSnBr_3$, and $CsSnI_3$. *Phys. Rev. B* **2013**, *88*, 165203.
(60) Monacelli, L.; Marzari, N. First-principles thermodynamics of $CsSnI_3$. *Chem. Mater.* **2023**, *35*, 1702−1709.
(61) Patrick, C. E.; Jacobsen, K. W.; Thygesen, K. S. Anharmonic stabilization and band gap renormalization in the perovskite $CsSnI_3$. *Phys. Rev. B* **2015**, *92*, 201205.
(62) Wang, H.; Tal, A.; Bischoff, T.; Gono, P.; Pasquarello, A. Accurate and efficient band-gap predictions for metal halide perovskites at finite temperature. *Npj Comput. Mater.* **2022**, *8*, 237.
(63) Leppert, L.; Rangel, T.; Neaton, J. B. Towards predictive band gaps for halide perovskites: Lessons from one-shot and eigenvalue self-consistent GW. *Phys. Rev. Mater.* **2019**, *3*, 103803.
(64) Filip, M. R.; Giustino, F. GW quasiparticle band gap of the hybrid organic-inorganic perovskite CH_3 NH_3 PbI_3: Effect of spin-orbit interaction, semicore electrons, and self-consistency. *Phys. Rev. B* **2014**, *90*, 245145.
(65) Yuan, F.; Folpini, G.; Liu, T.; Singh, U.; Treglia, A.; Lim, J. W. M.; Klarbring, J.; Simak, S. I.; Abrikosov, I. A.; Sum, T. C.; et al. Bright and stable near-infrared lead-free perovskite light-emitting diodes. *Nat. Photonics* **2024**, *18*, 170−176.
(66) Krishnamoorthy, T.; Ding, H.; Yan, C.; Leong, W. L.; Baikie, T.; Zhang, Z.; Sherburne, M.; Li, S.; Asta, M.; Mathews, N.; Mhaisalkar, S. G. Lead-free germanium iodide perovskite materials for photovoltaic applications. *J. Mater. Chem. A* **2015**, *3*, 23829−23832.
(67) Kammerlander, D.; Botti, S.; Marques, M. A. L.; Marini, A.; Attaccalite, C. Speeding up the solution of the Bethe-Salpeter equation by a double-grid method and Wannier interpolation. *Phys. Rev. B* **2012**, *86*, 125203.
(68) Wei, Q.; Ke, Y.; Ning, Z. Theoretical study of using kinetics strategy to enhance the stability of tin perovskite. *Energy Environ. Mater.* **2020**, *3*, 541−547.
(69) Tsuchiya, T.; Yamanaka, T.; Matsui, M. Molecular dynamics study of the crystal structure and phase relation of the GeO_2 polymorphs. *Phy. Chem. Miner.* **1998**, *25*, 94−100.
(70) Haines, J.; Leger, J. M.; Chateau, C.; Pereira, A. S. Structural evolution of rutile-type and $CaCl_2$-type germanium dioxide at high pressure. *Phy. Chem. Miner.* **2000**, *27*, 575−582.
(71) Bolzan, A. A.; Fong, C.; Kennedy, B. J.; Howard, C. J. Structural studies of rutile-type metal dioxides. *Acta Crystallogr. B* **1997**, *53*, 373−380.
(72) Armand, P.; Clement, S.; Balitsky, D.; Lignie, A.; Papet, P. Large SiO_2-substituted GeO_2 single-crystals with the α-quartz structure. *J. Cryst. Growth* **2011**, *316*, 153−157.
(73) Giorgi, G.; Fonseca, L.; Korkin, A.; Yamashita, K. Impact of the crystal structure of HfO_2 on the transport properties of model HfO_2/Si/HfO_2 silicon-on-insulator field-effect transistors: A combined DFT-scattering theory approach. *Phys. Rev. B* **2009**, *79*, 235308.
(74) Giorgi, G. Structural and electronic features of Si/$CH_3NH_3PbI_3$ interfaces with optoelectronic applicability: Insights from first-principles. *Nano Energy* **2020**, *67*, 104166.
(75) Da Silva, E. L.; Skelton, J. M.; Parker, S. C.; Walsh, A. Phase stability and transformations in the halide perovskite $CsSnI_3$. *Phys. Rev. B* **2015**, *91*, 144107.

https://doi.org/10.1021/acsami.6c00873
ACS Appl. Mater. Interfaces 2026, 18, 32782−32794

(76) Thiele, G.; Rotter, H. W.; Schmidt, K. D. Kristallstrukturen und phasentransformationen von caesiumtrihalogenogermanaten (II) $CsGeX_3$ (X= Cl, Br, I). *Z. Anorg. Allg. Chem.* **1987**, *545*, 148−156.
(77) Chang, J.; Jiang, L.; Wang, G.; Zhao, W.; Huang, Y.; Chen, H. Lead-free perovskite compounds $CsSn_{1-x}Ge_xI_{3-y}Br_y$ explored for superior visible-light absorption. *Phys. Chem. Chem. Phys.* **2021**, *23*, 14449−14456.
(78) Bokdam, M.; Sander, T.; Stroppa, A.; Picozzi, S.; Sarma, D. D.; Franchini, C.; Kresse, G. Role of polar phonons in the photo excited state of metal halide perovskites. *Sci. Rep.* **2016**, *6*, 28618.
(79) Howie, R.; Moser, W.; Trevena, I. The crystal structure of tin (II) iodide. *Acta Crystallogr. B* **1972**, *28*, 2965−2971.
(80) Marshall, K. P.; Walker, M.; Walton, R. I.; Hatton, R. A. Elucidating the role of the hole-extracting electrode on the stability and efficiency of inverted $CsSnI_3/C_{60}$ perovskite photovoltaics. *J. Mater. Chem. A* **2017**, *5*, 21836−21845.
(81) Giorgi, G.; Korkin, A.; Yamashita, K. Zirconium and hafnium oxide interface with silicon: Computational study of stress and strain effects. *Comput. Mater. Sci.* **2008**, *43*, 930−937.
(82) Van de Walle, C. G.; Martin, R. M. Theoretical study of band offsets at semiconductor interfaces. *Phys. Rev. B* **1987**, *35*, 8154.
(83) Volonakis, G.; Giustino, F. Ferroelectric graphene−perovskite interfaces. *J. Phys. Chem. Lett.* **2015**, *6*, 2496−2502.
(84) Quarti, C.; De Angelis, F.; Beljonne, D. Influence of surface termination on the energy level alignment at the CH3NH3PbI3 perovskite/C60 interface. *Chem. Mater.* **2017**, *29*, 958−968.
(85) Mallik, N.; Hajhemati, J.; Frégnaux, M.; Coutancier, D.; Toby, A.; Zhang, S.-T.; Hartmann, C.; Hüsam, E.; Saleh, A.; Vincent, T.; et al. Interface defect formation for atomic layer deposition of SnO2 on metal halide perovskites. *Nano Energy* **2024**, *126*, 109582.
(86) Lee, Y.; Lee, S.; Seo, G.; Paek, S.; Cho, K. T.; Huckaba, A. J.; Calizzi, M.; Choi, D.-W.; Park, J.-S.; Lee, D.; et al. Efficient planar perovskite solar cells using passivated tin oxide as an electron transport layer. *Adv. Sci.* **2018**, *5*, 1800130.

https://doi.org/10.1021/acsami.6c00873
ACS Appl. Mater. Interfaces 2026, 18, 32782−32794